Supplementary Information

Microbially-mediated aerobic oxidation of trace element-bearing pyrite in neutral-pH sandstone aquifer sediments

Lisa Haas[a,b], Matthew Ginder-Vogel[c], James J. Zambito IV[d], David Hart[b], and Eric E. Roden[a,*]

[a] University of Wisconsin, Department of Geoscience, 1215 West Dayton Street, Madison, WI 53706 USA

[b] Wisconsin Geological and Natural History Survey, 3817 Mineral Point Rd, Madison, WI 53705

[c] University of Wisconsin, Department of Civil and Environmental Engineering, Water Science Engineering Laboratory, 660 N. Park Street, Madison, WI 53706

[d] Beloit College, Department of Geology, 700 College Street, Beloit, WI 53511, USA

* Corresponding author: Eric E. Roden, eroden@geology.wisc.edu

E-mail addresses:, ldhaas@wisc.edu (L.D. Haas), mgindervogel@wisc.edu (M. Ginder-Vogel) zambitoj@beloit.edu (J.J. Zambito), david.hart@wisc.edu (D. Hart), eroden@geology.wisc.edu (E.E. Roden)

Supplemental Text: Pyrite oxidation model

Model development

The PHREEQC geochemical modeling software (Parkhurst and Appelo, 1999) was used to simulate the pyrite oxidation results for the reduced WF microcosms. The goal was to develop a calibrated batch model which could subsequently be employed in transport-reaction simulations using the 1-D fluid transport capabilities in PHREEQC (see Materials and Methods in the text). The aqueous phase solution composition (SOLUTION keyword in PHREEQC) was defined by the data given in Table S4, with adjustment of total dissolved inorganic carbon (2.5 mM) and alkalinity (5.0 mM) to reproduce the initial pH in the microcosms. The solution was assumed to remain in equilibrium with atmospheric O_2 (EQUILIBRIUM_PHASES in PHREEQC, consistent with the initial air headspace in the bottles and the periodic addition of air to the bottles during aqueous phase sampling.

The reactions included in the pyrite oxidation model are listed in Table S5. Pyrite oxidation (KINETICS and RATES keyword blocks in PHREEQC) was assumed to follow the pH- and dissolved oxygen-dependent, surface area-normalized rate law described in Williamson and Rimstidt (1994), as depicted in Manning et al. (2013):

$$r = k_k \cdot A_s$$

where r is the reaction rate of pyrite dissolution (e.g. mol g^{-1} s^{-1}), A_s is the pyrite surface area, and k_k is the the pH- and dissolved oxygen-dependent, surface area-normalized rate constant, with

$$k_k = k_s \cdot m_{DO}^{0.5} / m_{H^+}^{0.11}$$

where k_s is the surface area-normalized pyrite oxidation rate constant, and m_{DO} and m_{H+} are the molal dissolved O_2 and H^+ concentrations. All reactions were assumed to operate at constant temperature, and hence no temperature dependence was included in any of the model calculations reported here. The initial surface area of the natural pyrite (0.02 m^2 g^{-1}) was estimated based on the average dimension of the octahedra observed in the WF material (ca. 20 μm, see Fig. 7) and an assumed mineral density of 5 g cm^{-3} (www.mindat.org/min). The available pyrite surface area of the pyrite was assumed to scale downward with bulk pyrite loss according to a standard mineral dissolution function based on dissolution of ideal microspheres (Christoffersen and Christoffersen, 1976; Postma, 1993).

The rate function for pyrite oxidation added FeS_2, as a geochemical entity, to the system incrementally over time (according to the fifth-order Runge-Kutta numerical integration algorithm included in PHREEQC) during the simulation, after which the added reduced iron and sulfur in the mineral reacted to thermodynamic equilibrium with dissolved O_2 in the solution. Note that reaction of pyrite with soluble ferric iron (Fe^{3+}), a key pathway in low-pH pyrite oxidation (Nordstrom and Southam, 1997), was not explicitly included in the model, since the pH values obtained in our experiments were not low enough to allow for significant accumulation of Fe^{3+} ions. Rather, virtually all of the Fe(III) produced during FeS_2 oxidation was sequestered into the Fe(III) oxide mineral goethite, which was assumed to precipitate to equilibrium in the simulation.

A relatively "high surface area" (HSA), nano-crystalline form of goethite (EQUILIBRIUM_PHASES keyword in PHREEQC) was assumed to be produced during FeS_2 oxidation, based on a wealth of observations that such "nanogoethite" phases are the most common form of Fe(III) oxide present in sediments where pyrite oxidation takes place (Vanderzee et al., 2003). The HSA goethite was assumed to have a surface area (150 $m^2\ g^{-1}$) and thermodynamic properties (ΔG_f = -483 kJ mol^{-1}, which corresponds to a log K solubility product of $10^{-0.71}$) similar to those of synthetic goethite formed through oxidation of soluble ferrous iron in neutral-pH bicarbonate buffered solution (Roden, 2008). The abundance of surface sites (SURFACE keyword in PHREEQC) available for sorption of ions released during pyrite oxidation was defined by a universal mineral surface site density of 3.85×10^{-6} mol sites m^{-2} (Davis and Kent, 1990). The bulk abundance of such sites increased over time as result of Fe(III) oxide production during pyrite oxidation. Surface complexation constants for H^+, SO_4^{2-}, Ca^{2+}, and selected trace elements (illustrated here with Ni^{2+}) from Dzombak and Morel (1990) are included in the MINTEQ thermodynamic database (Table S5) and were engaged automatically in the PHREEQC simulations. The complexation constants for "weak" hydrous ferric oxide surface sites from Dzombak and Morel (1990) were used to model surface complexation on HSA goethite surfaces. A fractional amount of Ni-substituted pyrite (NiS_2) was assumed to be released during pyrite oxidation, where the fractional amount was based on the measured relative abundance of Ni in the reduced WF sediment (Table S2).

An initial quantity of dolomite was included in the simulation (EQUILIBRIUM_PHASES keyword) to represent the dominant solid-phase carbonate in the WF, with the amount (1.5 mmol L^{-1}) chosen based on the amount of Ca and Mg that accumulated in solution during the experiment (Fig. 4E). Carbonate dissolution was assumed to proceed to thermodynamic equilibrium throughout the simulations.

Pyrite oxidation rate constants

The only parameter subject to calibration was the surface area-specific rate constant for pyrite oxidation. This parameter was adjusted by trial-and-error to provide a reasonable fit to the measured sulfate vs. time data for the biotic and abiotic reduced WF microcosm experiments (Fig. A4). The estimated rate constant for biologically mediated pyrite oxidation ($10^{-7.8}$ mol m^{-2} s^{-1}) was ca. 25-fold higher for abiotic oxidation ($10^{-9.2}$ mol m^{-2} s^{-1}). These values were used as the for the single-cell REV reactive transport simulations.

The estimated surface area-normalized rate constant for abiotic oxidation of natural pyrite in the reduced WF sediment is ca. 10-fold lower than that for abiotic, oxygen-mediated oxidation of specimen pyrite ($10^{-8.19}$) reported in Williamson and Rimstidt (1994), and ca. 30-fold lower than the value estimated for oxidation of specimen pyrite in the oxidized (pyrite-depleted) WF sediment employed in a parallel study ($10^{-7.7}$ mol m^{-2} s^{-1}; data not shown). It should be noted here that microbial activity did not dramatically enhance the rate of specimen pyrite oxidation in this study, which points to a greater potential impact of microbial catalysis on pyrite oxidation in natural systems. Unfortunately, as discussed in Manning et al. (2013), it is difficult to translate our laboratory-derived rate constants to natural systems, where the available surface area of pyrite in situ is poorly constrained, and may not be accurately reflected by the size and reactivity of the pyrite octahedra (Fig. 7) examined in this study. Removal or lessening (e.g. through sediment grinding) of factors that may inhibit contact between dissolved oxygen (and microorganisms) and fresh pyrite (e.g. mineral coatings which ‘‘armor’’ mineral surfaces), as

well as an increase in the overall exposure of mineral grains to reactants compared to mineral grains embedded within cemented sediments, will almost certainly lead to accelerated experimental reaction rates. Manning et al. (2013) carefully acknowledged this problem, and dealt with it by adopting a lumped parameter called the ‘‘reactivity product’’ parameter defined as:

$$R_p = k_s A_s$$

where R_p is the bulk pyrite oxidation rate in units of mol/kg/s. Values for R_p were then estimated empirically using the sulfate concentration measured in the upper saturated zone (below the depth of pyrite oxidation) of their field study site, and the measured unsaturated zone oxygen profile. In this manner, they treated the unsaturated zone as a field-scale reactor in which the rate of pyrite oxidation (i.e. R_p) was inferred in a manner analogous to how we estimated rates constants for WF reduced sediment in our batch reactors. In contrast to the Manning et al. (2013) study, the field-scale simulations described here were not conducted to reproduce field measurements of sulfate abundance, but rather to assess the potential impact of biologically-enhanced pyrite oxidation on geochemical conditions in zone where aerobic groundwater impinges on reduced, pyrite-bearing sediment. Hence, we adopted the surface area-normalized pyrite oxidation rate constants and estimated pyrite reactive surface areas derived from the incubation experiments to drive pyrite oxidation in the single-cell REV reactive transport model.

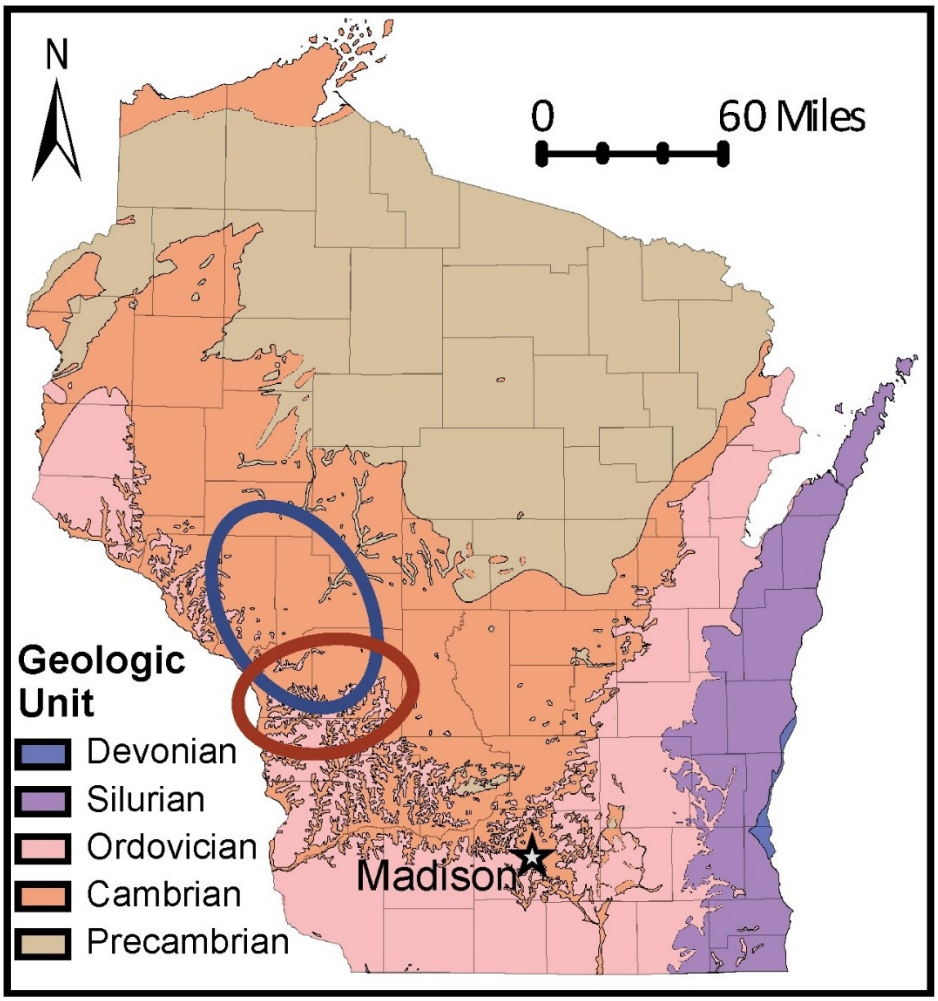

Fig. S1: Map showing major geological units in the state of Wisconsin, USA. Red and blue encircled areas on the inset map highlight where the tested wells and frac sand wash ponds are located, respectively.

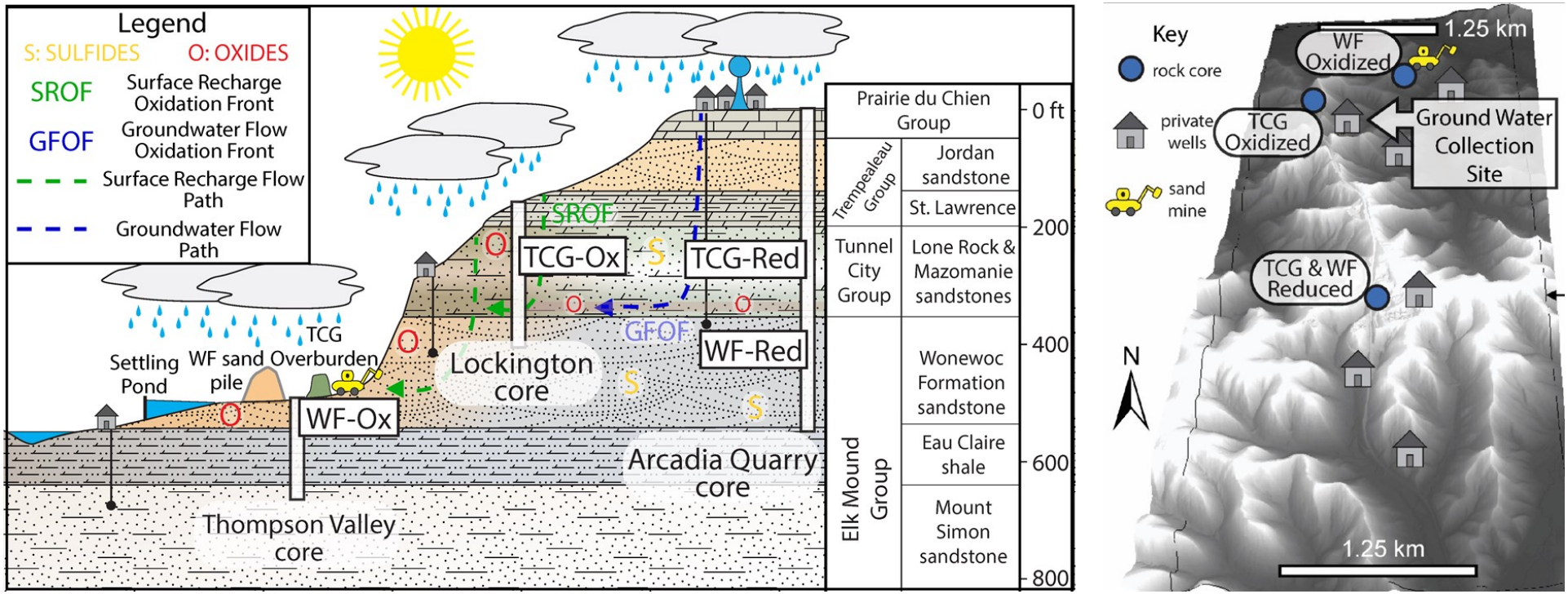

Fig. S2: Left: Generalized stratigraphy for the study area, showing locations of the drill cores and approximate depths from which the geological materials used in this study were obtained (modified from Fig. 1 in Zambito et al., (2022). Right: Map showing drill core locations in relation to landscape relief in the study area. Note that the left-right (east-west) orientation of the stratigraphic profile is reversed relative to the landscape relief map.

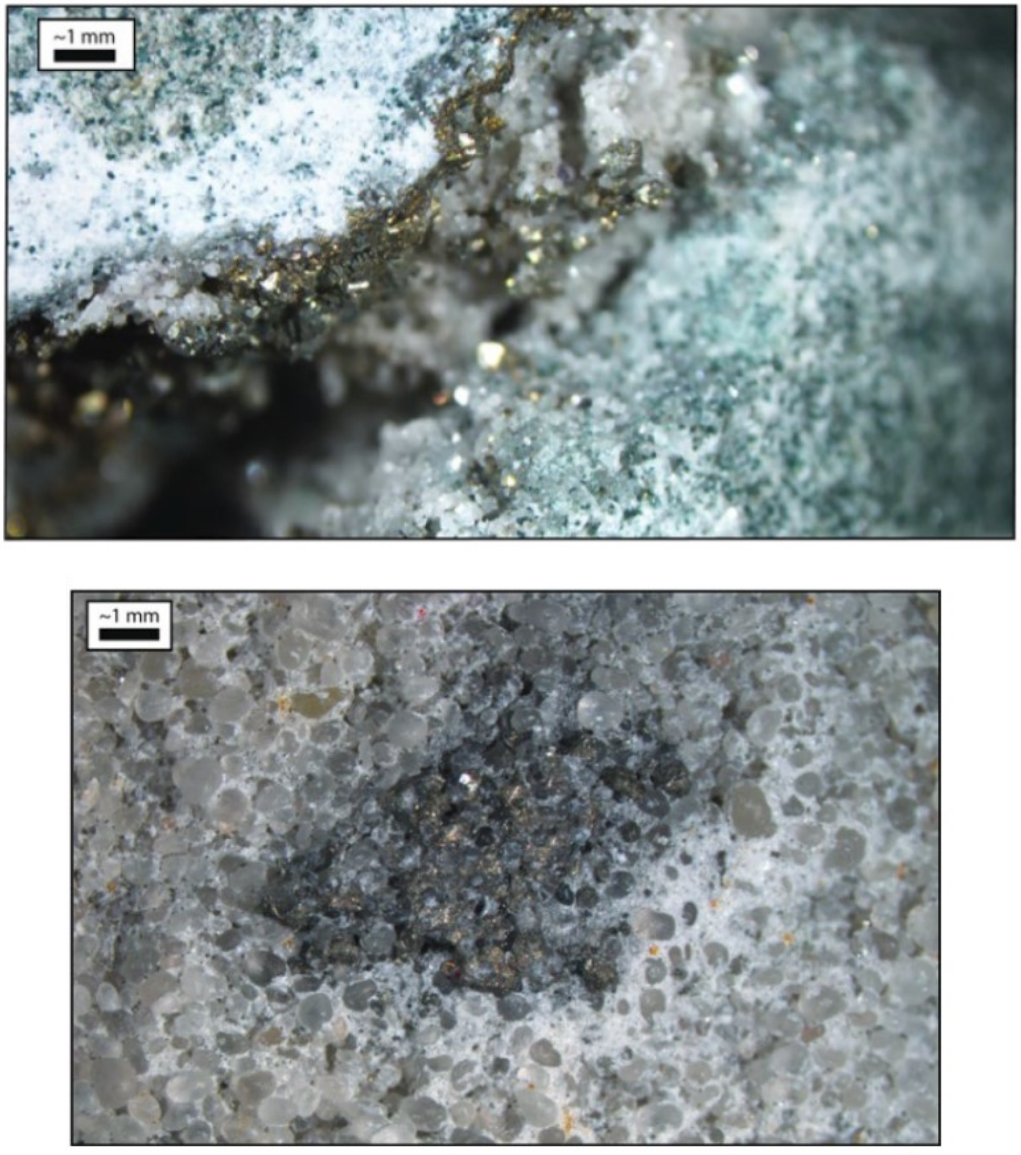

Fig. S3: Upper: magnified image of the Tunnel City Group rock core sample with pyrite lining the inside of a vugg, collected at about 186 feet depth (upper). Lower: magnified image of Wonewoc Formation rock core sample with abundant well-rounded quartz sand. Sample was collected from about 360 feet depth. The sulfide nodule is replacing an ca. 500 million-year-old worm burrow. Surrounding the pyritized burrow are sub-mm disseminated pyrite crystals.

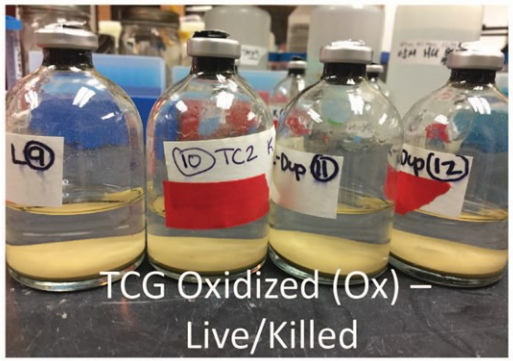

Biotic (Live, L)

5 g sediment +
5 mL groundwater

↓

Autoclave

↓

+ 45 mL groundwater

↓

Sterile sampling
over time

Abiotic (Killed, K)

5 g sediment +
50 mL groundwater

↓

Autoclave

↓

Sterile sampling
over time

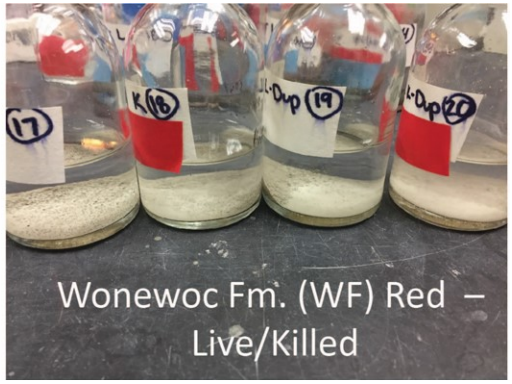

Fig. S4: Photos and diagram of microcosm set-up. The sediment added to the microcosms was pulverized and washed with distilled water to remove residual sulfate prior to addition to the reactors.

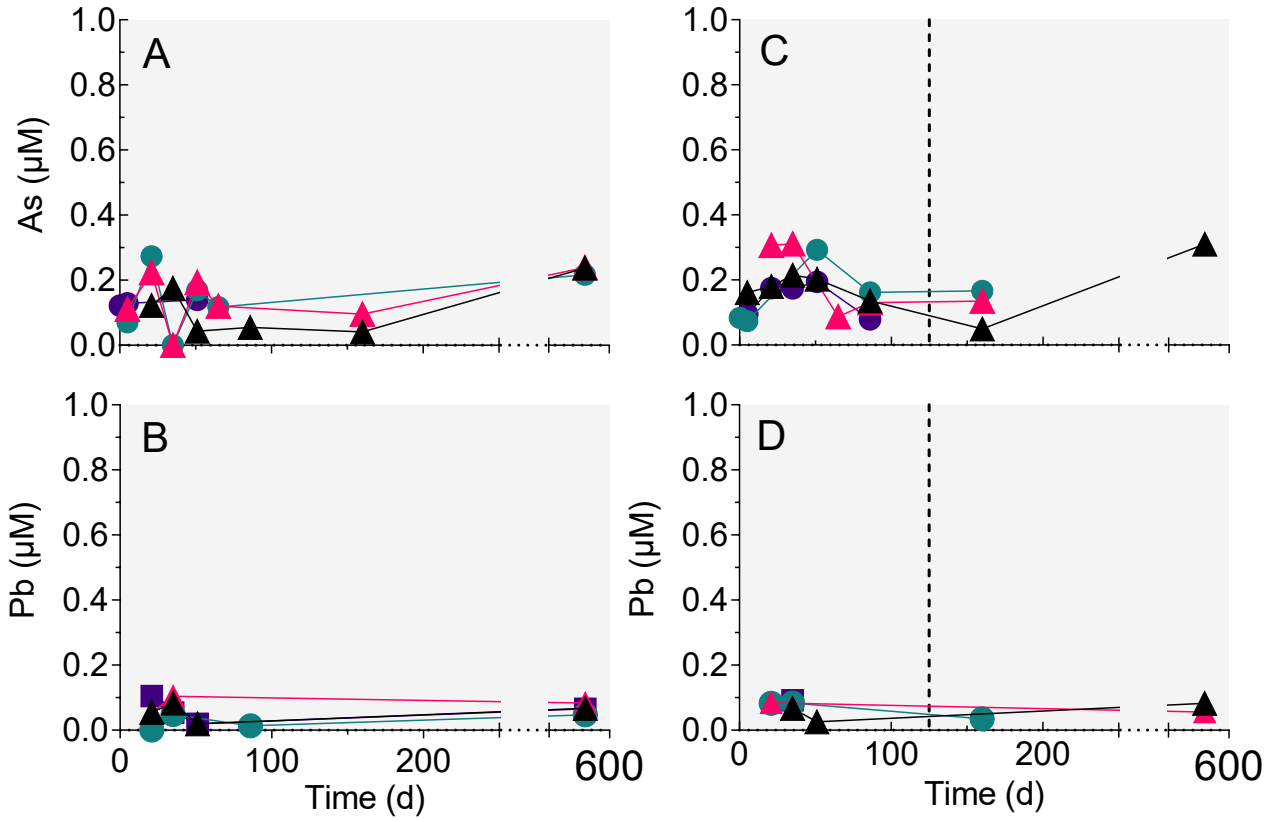

Fig. S5. Changes in aqueous-phase As (A, C) and Pb (B, D) in the reduced and oxidized TCG and WF sediment incubations. The values for biotic TCG-Red represent the average of the duplicate microcosms. All other data points are one sample of combined aqueous-phase treatment duplicates. Values below limit of detection of the analytical assay are not plotted. Dotted lines in right-hand panels mark halfway between the two time points when the biotic WF-Red reactors went acidic.

Table S1. Major element composition (% dry weight) aqua regia digestion, ICP-OES analysis, ALS Geochemistry, Reno, NV, USA) of Tunnel City Group (TCG) and Wonewoc Formation (WF) reduced (Red) and Oxidized (Ox) materials used in the microcosm experiments.

	Major Element									
Sample	**Si**	**Al**	**K**	**Ca**	**Mg**	**Fe**	**S**	**P**	**Ti**	**Description**
TCG-Red	36.2	1.34	1.8	10.7	6.01	2.55	0.5	0.092	0.064	Carbonate cemented glauconitic and feldspathic quartz sandstone with trace sulfur-based minerals
TCG-Ox	36.1	1.9	2.65	10.35	5.41	2.44	0.01	0.088	0.097	Carbonate cemented glauconitic arenite - with negligible sulfur based-minerals
WF-Red	46.2	0.18	0.21	0.3	0.01	0.73	0.82	0.008	0.014	Arenite with weakly silica and microcline cemented with trace sulfur-based minerals
WF-Ox	46.2	0.17	0.12	0.01	0.01	0.83	0.13	0.0038	0.01	Arenite with weakly silica and microcline cemented with negligible sulfur-based minerals

Table S2. Selected trace metal composition of Tunnel City Group (TCG) and Wonewoc (WF) formation materials used in the microcosm experiments.

	Trace Element Concentration (ppm)											
Material	**As**	**Cd**	**Co**	**Cr**	**Cu**	**Mn**	**Mo**	**Ni**	**Pb**	**Sr**	**V**	**Zn**
TCG-Red	2.8	0.01	5.9	11.6	7.7	1500	0.08	9.05	4.22	54.5	12	34.3
TCG-Ox	3.1	0.006	9.1	16.6	25.4	1090	0.17	13.25	9.96	51.4	14.5	5.6
WF-Red	0.6	0.005	0.74	2.3	8.2	5.6	0.09	4.04	2.97	11.65	3.2	1.2
WF-Ox	2.3	0.006	0.62	4.4	6.8	20.5	0.3	3.73	5.08	42.1	5.7	2.5

Table S3. Composition of groundwater used in the microcosm experiments (see Fig. S2 for sampling location).

Analyte	Value
pH	7.5
Alkalinity	5 mM
Cl^-	0.47 mM
NO_3^-	0.13 mM
SO_4^{2-}	0.26 mM
Al^{3+}	2.7 µM[1]
As^{5+}	0.061 µM[2]
Ba^{2+}	Below detection[2]
Ca^{2+}	1.4 mM
Co, Fe, Mn, Mo, Ni, Pb, Zn	Below detection[2]
Cu	0.13 µM[2]
K^+	0.016 mM
Mg^{2+}	0.69 mM
Na^+	1.9 mM
PO_4^{3-}	0.0049 mM
$Si(OH)_4$	0.17 mM
Sr^{2+}	0.29 µM

[1] Detection limit 0.015 ppm (0.53 µM)
[2] Detection limits < 0.01 ppm

Table S4. Aqueous and solid-phase concentrations used in the batch and single-cell REV reactive transport simulations. Aqueous phase concentration are those for the groundwater used in the microcosm experiments (Table S3), with the initial measured concentration of sulfate. The fluid composition listed for the REV simulation was used as both the initial condition in the REV and the composition of the fluid entering the REV.

Component	**Batch**	**REV**
pH	8.1	9.3
Alkalinity	5 mM	5 mM
CO_3^{2-}	2.5 mM[1]	5 mM[2]
NO_3^-	0.13 mM	0.13 mM
SO_4^{2-}	0.26 mM	0.35 mM
Al^{3+}	2.7 µM	2.7 µM
Ca^{2+}	1.4 mM	1.4 mM
K^+	0.016 mM	0.016 mM
Mg^{2+}	0.69 mM	0.69 mM
Na^+	1.0 mM	1.0 mM
Ni^{2+}	0.0	0.0
$Si(OH)_4$	0.17 mM	0.17 mM
Solid-phase components	**Initial value**	
FeS_2 (pyrite)	0.025 mol L H_2O^{-1}	1.44[3] mol L H_2O^{-1}
$CaMg(CO_3)$ (dolomite)	0.0015 mol L H_2O^{-1}	0.0875[2] mol L H_2O^{-1}
FeOOH (goethite)	0.0 mol L H_2O^{-1}	0.0 mol L H_2O^{-1}

[1] Specified to produce initial pH = 9.3 in the microcosm reactors. The elevated pH in the microcosms relative to the groundwater was caused by degassing of CO_2 during preparation.
[2] Specified to produce initial pH = 7.5 in the groundwater (Table S3).
[3] Scaled from the batch value assuming 30% in situ porosity.

Table S5. Reactions included in the pyrite oxidation model.

Pyrite oxidation: $FeS_2(s) + 3.75O_2 + 0.5H_2O \rightarrow Fe^{3+} + 2SO_4^{2-} + H^+$
Fe(III) oxide precipitation: $Fe^{3+} + 3H_2O \leftrightarrow FeOOH(s) + 3H^+$
Dolomite dissolution: $CaMg(CO_3)_2(s) \leftrightarrow Ca^{2+} + Mg^{2+} + 2CO_3^{2-}$
Surface complexation by HSA goethite (HSA_Gt)[1]: $HSA\_GtOH = HSA\_GtO^- + H^+$ log K = -8.93 $HSA\_GtOH + H^+ = HSA\_GtOH_2^+$ log K = 7.29 $HSA\_GtOH + Ca^{2+} = HSA\_GtOCa^+ + H^+$ log K = -5.85 $HSA\_GtOH + H^+ + SO_4^{2-} = HSA\_GtSO4^- + H_2O$ log K = 7.78 $HSA\_GtOH + SO_4^2 = HSA\_GtSO4^{2-}$ log K = 0.79 $HSA\_GtOH + Ni^{2+} = HSA\_GtONi^+ + H^+$ log K = -2.5

[1] log K values are those for "weak" hydrous ferric oxide surface sites from Dzombak and Morel (1990).

Table S6. Parameters used in the batch and single-cell REV reactive transport models of pyrite oxidation. The only adjustable parameter in the batch simulation models was k_s (see Supplemental Text).

Parameter	Description	Value	Units
k_s	surface area-normalized pyrite oxidation rate constant	$10^{-7.8}$ (biotic), $10^{-9.2}$ (abiotic)	mol m^{-2} s^{-1}
A_s	Pyrite surface area	0.02	m^2 g^{-1}
K_{sp}, HSA goethite	Solubility product for high surface area (HSA) goethite	$10^{-0.71}$	
K_{sp}, dolomite	Solubility product for dolomite (default value in MINTEQ database)	$10^{-0.17}$	
Cell length[1]/ Time step[2]	Groundwater flow rate	1-10 (3.65-36.5)	cm d^{-1} (m yr^{-1})
	Initial fuid composition (batch & REV)	Table S4	
	Influent concentration for REV reactive transport simulation	Table S4	

[1] Cell length in the ADVECTION keyword block on PHREEQC, fixed at 1 m for the single-cell REV reactive transport simulations.
[2] Time step for each fluid advection "shift" in the ADVECTION keyword block on PHREEQC.

References

Christoffersen, J., and M. R. Christoffersen. 1976. The kinetics of dissolution of calcium sulphate dihydrate in water. J. Crystal Growth 35:79-88.

Davis, J. A., and D. B. Kent. 1990. Surface complexation modeling in aqueous geochemistry. In M. F. Hochella, and A. F. White (eds.). Mineral-water interface geochemistry, pp. 177-260. Mineralogical Society of America, Washington, DC.

Dzombak, D. A., and F. M. M. Morel. 1990. Surface Complexation Modeling: Hydrous Ferric Oxide. John Wiley & Sons, New York.

Manning, A. H., P. L. Verplanck, J. S. Caine, and A. S. Todd. 2013. Links between climate change, water-table depth, and water chemistry in a mineralized mountain watershed. Appl. Geochem. 37:64-78.

Nordstrom, D. K., and G. Southam. 1997. Geomicrobiology of sulfide mineral oxidation. In J. F. Banfield, and K. Nealson (eds.). Geomicrobiology: Interactions Between Microbes and Minerals, pp. 361-382. Mineralogical Society of America, Washington, DC.

Parkhurst, D. A., and C. A. Appelo. 1999. User's guide to PHREEQC (Version 2). Water-Resources Investigation Report 99-4259.

Postma, D. 1993. The reactivity of iron oxides in sediments: a kinetic approach. Geochim. Cosmochim. Acta 57:5027-5034.

Roden, E. E. 2008. Microbiological controls on geochemical kinetics 1: Fundamentals and case study on microbial Fe(III) reduction. In S. L. Brantley, J. Kubicki, and A. F. White (eds.). Kinetics of Water-Rock Interactions, pp. 335-415. Springer, New York.

Vanderzee, C., D. R. Roberts, D. G. Rancourt, and C. P. Slomp. 2003. Nanogoethite is the dominant reactive oxyhydroxide phase in lake and marine sediments. Geology 31:993-996.

Williamson, M. A., and J. D. Rimstidt. 1994. The kinetics and electrochemical rate-determining step of aqueous pyrite oxidation. Geochim. et Cosmochim Acta 58:5443-5454.